Precision Agriculture (2023) 24:1049–1071
https://doi.org/10.1007/s11119-022-09987-z

Quantification of rice spikelet rot disease severity at organ scale with proximal imaging spectroscopy

Bowen Xue[1] · Long Tian[1] · Ziyi Wang[1] · Xue Wang[1] · Xia Yao[1] · Yan Zhu[1] · Weixing Cao[1] · Tao Cheng[1]

Accepted: 29 December 2022 / Published online: 9 January 2023

Abstract

Spikelet diseases pose severe threats to crop production and crop protection requires timely evaluation of disease severity (DS). However, most studies have only investigated the spikelet diseases within a short period of crop growth. Few have examined the consistency in DS monitoring accuracy across growth stages. This study aimed to investigate the differences in spectral responses among growth stages and to develop a spectral index (SI), rice spikelet rot index (RSRI), for multi-stage monitoring of the rice spikelet rot disease. Proximal hyperspectral images were collected over spikelets with various levels of DS at heading, anthesis, and grain filling stages. The reflectance was related to the DS extracted from concurrent high-resolution RGB images. The proposed RSRI was evaluated for the DS estimation and lesion mapping across growth stages in comparison with existing SIs. The results demonstrated that the spectral responses to DS in the green and near-infrared regions for filling were weaker than those for anthesis, and blue bands were necessary in DS quantification for early infection. The RSRI-based models exhibited the best validation accuracy for heading and the most consistent performance across growth stages as comparison to other SIs (Heading: $R^2 = 0.65$; anthesis: $R^2 = 0.84$; filling: $R^2 = 0.78$). Moreover, RSRI-based DS maps exhibited the best lesion identification for slightly, mildly, and severely infected spikelets. This study suggests that RSRI could be promising in breeding and crop protection as a novel index for DS estimation regardless of the spikelet ripening effect.

Keywords Hyperspectral imaging · Rice spikelet rot disease · Spectral index · Disease severity · Early infection · Ripening

Abbreviations

DS	Disease severity
RSRD	Rice spikelet rotdisease
HSI	Hyperspectral image
VNIR	Visible andnear-infrared
NIR	Near-infrared

✉ Tao Cheng
tcheng@njau.edu.cn

[1] Nanjing Agricultural University, Nanjing, Jiangsu, China

DD Double difference
SI Spectral index
RSRI Rice spikelet rotindex

Introduction

The stable and sustainable production of the rice industry has been hampered by various stressors from diseases and pests to environmental issues, among which the fungal diseases are considered as major threats to rice yield and quality (Jagadish et al., 2015; Liu et al., 2014). Rice spikelet rot disease (RSRD), a fungal disease caused mainly by *Fusarium proliferatum*, is an emerging disease in rice planting areas of eastern Asia prompted by a combination of changes in rice variety, crop management, and environment factors (Huang et al., 2011a). RSRD is highly contagious, and it degrades the rice yield and quality significantly due to the harmful and toxigenic pathogens. However, RSRD could only be effectively prevented in a brief period with fungicides (Huang et al., 2011b; Lei et al., 2019). Thus, an efficient and accurate estimation of the disease severity (DS) at the early infection stage is crucial for restraining the disease spread and minimizing the potential damage to rice production. However, the conventional approaches based on visual inspection of disease occurrence are subjective, labor-intensive, and inefficient. In addition, the infected spikelets with moderate lesions can hardly be identified visually under field conditions (Oerke, 2020; Zhang et al., 2019). In contrast, remote sensing can be used as an efficient and non-destructive approach to monitoring crop diseases.

A number of studies have used hyperspectral remote sensing to detect crop diseases across various scales (Mahlein et al., 2019a; Meng et al., 2022; Poblete et al., 2020; Ren et al., 2021). They determined the spectral features sensitive to different diseases and developed approaches to identifying the diseased samples or classifying DS levels. Moreover, several studies have unveiled the feasibility of disease detection at pre-visual and early stages (Gold et al., 2020; Tian et al., 2021; Zarco-Tejada et al., 2018), which could facilitate crop protection implementations to prevent the spread of pathogens. For example, Tian et al. (2021) identified leaves infected by rice blast for asymptomatic and early infection stages using a few spectral features. However, little attention has been paid to the detection of spikelet diseases in crops. Compared with foliar organs, spikelets are more difficult to be observed in contact probes with non-imaging spectrometers due to the three-dimensional morphology. Non-imaging spectral measurements are also limited in fine-scale monitoring with the lack of spatial details. Given its capacity of capturing spectral and spatial details, close-range imaging spectroscopy is well suited for monitoring individual organs and identifying lesion locations. Recently, several studies have reported on the application of imaging techniques to gather the integrated optical properties of reproductive organs for disease detection or pathology investigation (Gao et al., 2019; Huang et al., 2015; Mahlein et al., 2019a; Zhang et al., 2020b). However, relevant studies using imaging spectroscopy still focused on disease identification or multi-level DS classification. For example, Huang et al., (2015) classified the hyperspectral images of individual spikelets into six classes of DS using bag-of-words features and a support vector machine. Few studies have investigated the spectral responses to diseases explicitly or examined the spatial information to track the disease development. More research is in urgent need to uncover the spectral signatures and map the lesion distribution to enable an improved reference for pathology and crop protection.

Recently, the demand for accurate disease evaluation has been rising in crop breeding, crop phenomics, and precision agriculture (Mahlein et al., 2019b; Singh et al., 2021). Physically-based approaches are advantageous in disease monitoring with model inverted crop functional traits including pigment and water contents (Hornero et al., 2020; Morel et al., 2018), but the high computational cost and model complexity has hindered the operational efficiency and simplicity. In terms of practical efficiency, feature engineering is favorable in extracting simplified spectral indicators sensitive to the disease condition. A number of studies have used feature extraction methods including spectral indices (SIs), derivative analysis, and continuous wavelet analysis in the spectral monitoring for crop diseases (Mahlein et al., 2013; Huang et al., 2015; Kochubey & Kazantsev, 2012; Tian et al., 2021). Among those methods, the use of SIs constructed with a small number of bands represents the most common way of disease monitoring (Huo et al., 2021; Ren et al., 2021; Zhang et al., 2020b). Yet, different pathogen–host interactions result in specific spectral responses across wavelengths covering visible, near-infrared, and shortwave infrared ranges (Zhang et al., 2019). This implies that specific SIs should be developed for various crop diseases for optimal monitoring performance. For instance, Ren et al. (2021) proposed a SI for the quantification of disease severity in wheat yellow rust and achieved higher accuracy than existing ones for both leaf and canopy scales. To date, no SIs have been constructed specifically for capturing the spectral responses to RSRD and quantifying the DS levels of this disease.

Since rice grain ripening also occurs during the period of RSRD development, the spectral response to physiological ripening would be mixed up with that to the biotic disease. However, previous studies only measured the stressed spikelets from a specific growth stage (Zhang et al., 2020b) or a short period after inoculation and did not cover the ripening process. Considering the spectral variation across all wavelengths with spikelet ripening (Feng et al., 2022; Zhou et al., 2017), it becomes imperative to investigate the consistency of disease-sensitive SIs across multiple stages from heading to grain filling. Although the spectral response to mild infection may be more susceptible to spikelet ripening, few studies have been devoted to spikelet disease monitoring at the early infection stage (e.g., heading). Several studies suggested that the spectral variation in diseased crops with phenological changes could be characterized by using multiple spectral features (Ruan et al., 2021; Zheng et al., 2021). Nevertheless, this operation would include extra burdens of feature engineering and model parameterization. Therefore, it is important to evaluate the feasibility of constructing a SI sensitive to RSRD from the early infection stage and to multiple later stages.

The overall goal of this research was to construct a new index suitable for RSRD quantification across growth stages, especially for the early infection stage. The specific research objectives were to determine the spectral responses of rice spikelets to RSRD over multiple growth stages with close-range imaging spectroscopy, to construct a new spectral index for universal quantification of RSRD severity across multiple growth stages, and to evaluate the new index in DS quantification and mapping in comparison with existing SIs.

Materials and methods

Experiment setup

The plot trial experiments for RSRD monitoring were conducted at the Pailou Experimental Station of Nanjing Agricultural University, Jiangsu province of China (31° 57′ N, 118° 51′ E). For the convenience of instruments setting, cement pools filled with field soil on the ground were used as experimental plots. There were 24 plots in the same size of 2 m × 3 m (Fig. 1). The experiments were implemented under the same setting except for rice variety in the rice seasons of 2019 and 2020. To keep consistency with the management of field practices, the basal nutrition fertilizers (Nitrogen, 150 kg ha^{-2}; P_2O_5, 135 kg ha^{-2}; and K_2O, 18.3 kg ha^{-2}) were applied ahead of transplanting. Then a topdressing of fertilizer (Nitrogen, 150 kg ha^{-2}) was carried out during the tillering stage. The rice crops were transplanted in a high density (0.1 and 0.15 m spacing in rows and columns, respectively) to create the high humidity environment required by RSRD infection and development.

Since Japonica varieties with plump and compact spikelets are more susceptible to RSRD (Huang et al., 2011a; Lei et al., 2019), eight Japonica varieties commonly cultivated in Jiangsu were selected (2019: Wuyungen 23, Wuyungeng 24, Wuyungeng 7, and Nangeng 44; 2020: Yangnong 1, Nangeng 9108, Nangeng 5055, and Huaidao 5). The RSRD occurred naturally in the plots in both 2019 and 2020.

Data collection and pre-processing

To avoid the severe obstruction from spikelets and leaves in plots and to increase the measurement efficiency, infected spikelets were removed from rice plants for in-situ imaging spectroscopy data collection around noon on cloudless days at the heading, anthesis, and filling stages. Part of the stalk was removed along with the spikelet to ensure the integrity of each sample. After removing, the fresh samples were moved to a gantry platform landed near the plots. During each measurement under the gantry, a total of five to eight spikelets were placed on a stool with a black panel underneath and a spectralon beside (Analytical Spectral Devices, Boulder, CO, USA). The reflectance for the black and white panels are 3% and 99.9%, respectively, in the visible and near-infrared (VNIR) regions. A digital single-lens reflex camera (EOS 80D, Canon, Tokyo, Japan) and a push-broom hyperspectral imager (GaiaField-V10E, Jiangsu Dualix Spectral Image Technology Co. Ltd, Nanjing, China) were mounted on the automatic linear-scanning system (HSIA-MScope-X, Jiangsu

Fig. 1 A map of the experimental area with the setup of trial plots for four varieties in 2019 (V1: Wuyungen 23, V2: Wuyungeng 24, V3: Wuyungeng 7, V4: Nangeng 44) and another four in 2020 (V1: Yangnong 1, V2: Nanggeng 9108, V3: Nangeng 5055, V4: Huaidao 5)

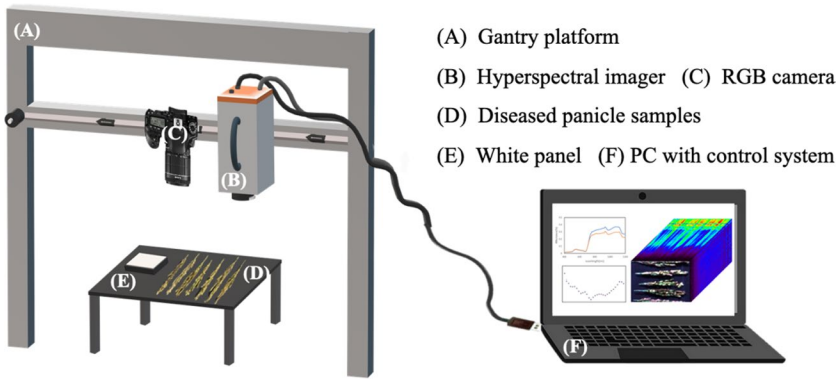

Fig. 2 Experimental setup for acquiring RGB and hyperspectral images of the rice spikelets under sunlight conditions

Table 1 A summary on the number of spikelet samples with RSRD infections for various stages in 2019 and 2020

Year	Heading	Anthesis	Filling
2019	0	123	29
2020	57	38	155
2019 and 2020	57	161	184

Dualix Spectral Image Technology Co. Ltd, Nanjing, China). The lifting height range is 250 ~ 1800 mm and the scanning distance is 1800 mm (Fig. 2). Furthermore, RGB photos and hyperspectral images (HSIs) were captured synchronously in the orthographic direction for consistent light conditions.

The RGB photos were collected via the remote control of the camera shutter. The camera was toggled to A^+ mode for automatic modification of the exposure time and the image quality was set to the maximum resolution of 6000 × 4000 pixels. The HSIs were acquired by the laptop software controlling the platform system. The distance between the hyperspectral lens and rice spikelets was kept at 0.4 m. Equipped with a lens of 42.8°, the HSI camera achieved a spatial resolution of 0.45 mm at this distance with 256 bands in a sampling interval of 2.5 nm over a range of 361–1011 nm. Since the optical aperture was fixed in the camera, the incident light was not consistent during the glit pushing. To strengthen the light consistency, image scanning was completed with the horizontal motor of the gantry instead of the internal push-broom module. In addition, a piece of grid paper was used for the manual adjustment on the motor speed and focal length to ensure non-distorted and clear hyperspectral frames. The exposure time of the HSI camera was set to 0.4 s manually to prevent overexposure for the spectralon at noon. These measurements covered a total of 401 spikelets for the 2 years (Table 1).

The reflectance of HSIs was derived from the original digital number values and then denoised using the Minimum Noise Fraction transformation (Zhou et al., 2018). The spectral interval of HSIs was resampled to 1 nm for the convenience of spectral processing. Only bands from 450 to 800 nm were used for spectral analysis due to the low signal-to-noise ratio outside this range. The overall region of each spikelet was cropped out manually in ENSI 5.3 (Exelis Visual Information Solutions, Boulder, CO, USA). The reflectance at band 760 nm was applied to mask out the background by setting a threshold of 0.2. Then

the spikelet regions were refined by removing the noise pixels with morphology methods. At last, the average reflectance of each spikelet was derived for the subsequent analysis. Spectral resampling and connected domain removal were conducted with the scipy package (https://scipy.org/) and the skimage package (https://scikit-image.org) in python 3.

Methodology

This research proposed a method for constructing a SI specifically for RSRD severity quantification by spectral analysis and band selection with DS reference extracted from RGB images. This method adopted multi-growth-stage spectra in band selection to ensure the stable performance and it included four steps: (1) determination of the SI form to characterize the main spectral responses; (2) selection of sensitive bands for multiple growth stages based on correlation analysis and correlation domain separation; (3) evaluation of the proposed SI in comparison with existing SIs in the DS quantification and lesion mapping.

Extraction of disease severity reference

Previous studies mainly applied qualitative DS standards to label the infected samples by visual inspection (Huang et al., 2015; Kobayashi et al., 2016). Such qualitative investigations might be inadequate for disease monitoring in precision agriculture (Mahlein et al., 2019b). To make up for the low efficiency and accuracy of human vision in DS quantification, a method was developed to automatically extract the DS reference data from the RGB images using color space conversion and dynamic threshold segmentation (Fig. 3B).

First, each sample was cropped from the RGB images and grouped with the corresponding spikelet HSI according to the sequence of measurement and visual matching. Then, the color space conversion was used to strengthen the contrast of each RGB

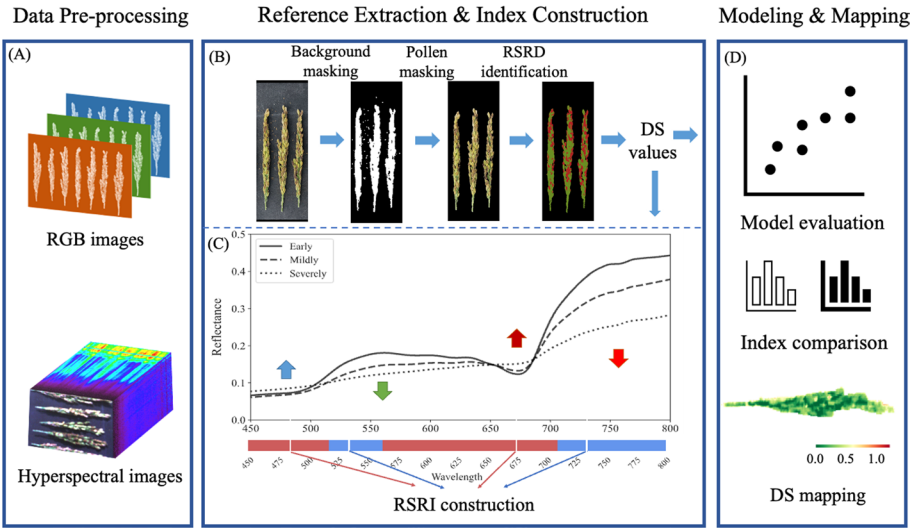

Fig. 3 Technical flowchart of the procedures for RSRI development, DS quantification and DS mapping (**A** Data pre-processing, **B** DS reference extraction, **C** Index construction, **D** Modeling and mapping)

image given the close brightness between the background and RSRD lesions. The Lab color space, which is barely influenced by light conditions or sensors (Gonzalez & Woods, 2002), was chosen for background removal and RSRD lesion identification. This space was a color-opponent space with the dimension 'L' for lightness and 'a' and 'b' for color-opponent dimensions. The 'b' values represented the true neutral gray values of yellow/blue opponent colors, which means 'b' was suitable for separating spikelets from the background. The 'a' values represented the true neutral gray values of red/green opponent colors, which means 'a' was suitable for separating infected pixels from healthy ones. Traditional thresholding methods often separate all pixels in the whole image with a single value (Gonzalez & Woods, 2002). However, the colors of severely and early infected pixels were close to the background and the healthy regions, respectively. Spikelets with advanced maturity were also in deep color close to lesions and backgrounds. This meant the global thresholding method would not be applicable for accurate extraction of spikelet lesions. In contrast, the local thresholding, also known as adaptive or dynamic thresholding, segments subregions with different thresholds to resist noise or color unevenness (Gonzalez & Woods, 2002). Dynamic methods could perform better than global ones regardless of growth stages or disease severity.

After the background removal with channel 'b' and local thresholding, a morphological refinement was conducted to remove the small components of isolated noise (the minimum connected component was set to five thousand pixels). Next, spikelet pixels were separated into infected and healthy ones using channel 'a' and the local thresholding. The subregion size for local thresholding was adjusted by visual comparisons between the identification results and raw RGB images. DS was calculated according to the pixel count in the following formula:

$$DS = \frac{n_d}{N} \tag{1}$$

where DS represents the RSRD lesion proportion of each spikelet, n_d and N are the numbers of diseased pixels and all pixels of each sample, respectively. It should be noted that the spatial correspondence of RGB images to HSIs was not considered in this study. The DS value was applied as observed disease severity for each sample at organ scale rather than pixel scale. This workflow was implemented using the aforementioned skimage package.

Proposed and existing spectral indices

The spectral indices for various diseases should be theoretically specific for certain plant-host interactions since different hosts with various infections could exhibit distinguishable spectral responses (Mahlein, 2016; Zarco-Tejada et al., 2021). Given this specificity, the rice spikelet rot index (RSRI) was constructed to express the unique spectral signatures for RSRD. The spectral profile over the VNIR region gradually flattened with the disease development. To increase the sensitivity of the proposed feature, multiple bands were combined to represent the flattened trend in the reflectance curves (Fig. 3C). The form of the double-difference (DD) index was then selected to describe the variation intensity. In addition, DD-form indices were found insensitive to noises of constant and linear trends including the sunlit intensity variation according to Li et al. (2019). Hence, the DD form should be suitable for the construction of disease indices with in-situ reflectance spectra:

$$DD = \frac{\left(R_{\lambda 2} - R_{\lambda 1}\right)}{\left(R_{\lambda 3} - R_{\lambda 2}\right)} \tag{2}$$

where $R_{\lambda 1}$, $R_{\lambda 2}$, and $R_{\lambda 3}$ are the reflectance of sensitive bands for the absorption valleys or reflectance peaks in incremental order of wavelength. The severer the DS, the more flattened the spectral curve and the closer the DD value to one.

To determine the sensitive bands for SI construction, a feature selection pipeline was applied including three steps as follows. First, the Spearman correlation per band was built between the reflectance and DS values over calibration samples (details about the sample division can be found in accuracy assessment). Spearman analysis was selected because the DS values in this study did not fit a normal distribution. To locate the different response regions, the correlation domains were constructed at the second step by separating the wavelength into positive and negative domains. Small domains covering less than five bands were discarded to ensure the robustness of band selection. Third, the bands with the strongest correlation of each domain were selected to form a number of alternative features on the correlation domains (Fig. 4). The aforementioned selection was conducted with the samples for heading, anthesis, and filling, respectively. For ensuring consistent sensitivity of the RSRD index, the common bands sensitive to RSRD severity for all stages were primarily selected in the red and NIR regions. To strengthen the sensitivity for the early stage of disease, three representative bands retained for the heading stage (the earliest infection stage) were used to construct three candidate indices. Determination coefficient (R^2) values were then derived with the calibration set to assess the DS quantification of each candidate. The feature with the maximum R^2 was determined to finalize the RSRI equation as below:

$$RSRI = \frac{\left(R_{675} - R_{454}\right)}{\left(R_{740} - R_{675}\right)} \tag{3}$$

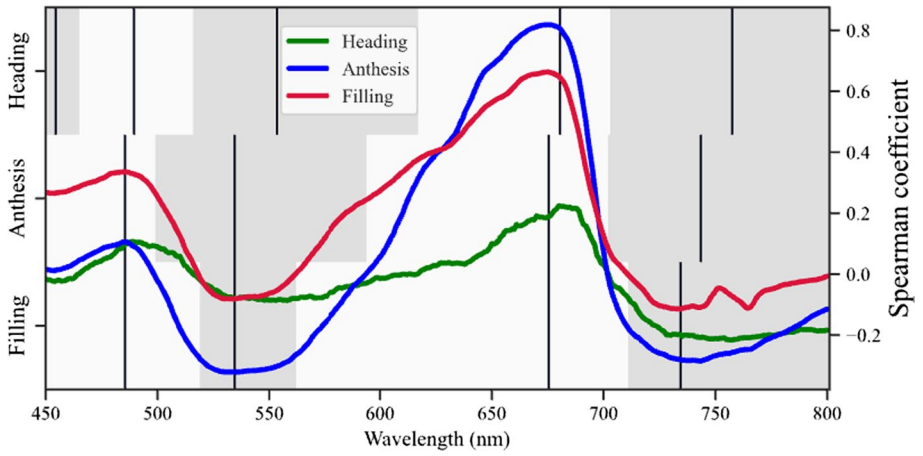

Fig. 4 Spearman correlation coefficients between disease severity (DS) and reflectance at wavelengths from 450 to 800 nm for various growth stages (green: heading, blue: anthesis, red: filling). Grey and white backgrounds represent negative and positive correlations, respectively. A vertical line in black corresponds to the maximum coefficient in each of the grey or white correlation domains (top row: heading, middle row: anthesis, bottom row: filling)

Table 2 Spectral indices used in this study

Index	Acronym	Formulation	References
Normalized difference vegetation index	NDVI	$(R_{NIR}-R_R)/(R_{NIR}+R_R)$	Rouse et al. (1974)
Photochemical reflectance index	PRI670	$(R_{670}-R_{531})/(R_{670}+R_{531})$	Gamon et al. (1992)
Normalized pigments index	NPCI	$(R_{680}-R_{430})/(R_{680}+R_{430})$	Peñuelas et al. (1993)
Plant senescence reflectance index	PSRI	$(R_{678}-R_{500})/R_{750}$	Merzlyak et al. (1999)
Chlorophyll/carotenoid Index	CCI	$(R_{531}-R_{645})/(R_{531}+R_{645})$	Gamon et al. (2016)
Rice Spikelet rot index	RSRI	$(R_{675}-R_{454})/(R_{740}-R_{675})$	This study

R_λ represents the reflectance at band λ

where R_{454}, $R_{675,}$ and R_{740} are the reflectance values at wavelengths of 454 nm, 675 nm, and 740 nm, respectively.

After sorting the R^2 of linear regressions for the commonly used SIs for vegetation stress monitoring as summarized in Tian et al. (2021), the five top-ranking SIs (NPCI, CCI, PRI670, PSRI, and NDVI) were adopted for comparison with RSRI (Table 2). Slightly, mildly, and severely diseased samples in a total of three spikelets were selected for the mapping comparison from the heading, anthesis, and filling stages, respectively. Next, the DS-SI relationships were applied to the HSIs of demonstration samples to map the disease distribution. A post-processing was used to mask the estimated DS values beyond the range from 0 to 1 by a piecewise function as follows:

$$x\prime = \begin{cases} 0, & x < 0 \\ min(x, 1), & x \geq 0 \end{cases} \tag{4}$$

where x is the estimated DS from SI-based models and x' is the post-processed DS for DS mapping. Given the unavailability of pixel-level reference DS for HSIs, the DS maps were compared with the RGB images, whose color shades could provide a general reference for RSRD severity.

Accuracy assessment

Due to the constraint by the infection and development of RSRD, the number of diseased spikelets was remarkably unbalanced for different growth stages over the experiment periods in 2019 and 2020 (Table 1). Thus, all samples from the 2 years were pooled up to conduct the RSRI construction, model calibration, and model validation. The pooled dataset was randomly divided into calibration (60%) and validation (40%) sets. Linear models were used to fit the relationships between DS and SIs. The quantification performance was evaluated in terms of the coefficient of determination (calibration R^2 and validation R^2), root mean square root (RMSE), and bias (Bias). The average R^2, RMSE, and bias values over 100 evaluation iterations were derived as below to assess the performance of SIs in DS estimation:

$$R^2 = 1 - \frac{\sum_i \left(y_i - y_i'\right)^2}{\sum_i \left(y_i - \bar{y}\right)^2} \tag{5}$$

$$RMSE = \sqrt{\frac{\sum_i \left(y_i - y_i'\right)^2}{n}} \tag{6}$$

$$Bias = \frac{\sum_i \left(y_i - y_i'\right)}{n} \tag{7}$$

where y_i and y_i' are the reference and estimated DS for spikelet sample i, respectively. $\bar{y}$ is the arithmetic mean of the DS value and n is the number of samples for each stage.

Results

Spectral responses of rice spikelets to RSRD

The reflectance spectra of RSRD infected rice spikelets changed with DS levels across all the VNIR spectral regions for the heading, anthesis and filling stages (Fig. 5). Overall, the reflectance variations of infected spikelets were similar over these stages, which included a weakening of the green peak, a strong increase in the red region, and a collapse in the near-infrared (NIR) region. There was also an increase in the blue regions and a shifting of the red edge towards short wavelengths with RSRD development. Additionally, the slope across the NIR region became more inclined with higher levels of DS.

While the spectral changes for heading were modest with the limited DS range (Fig. 5A), the anthesis stage exhibited the strongest spectral responses among all three stages (Fig. 5B). Specifically, responses in the blue and red regions were the strongest for filling compared with the rest stages. The reflectance of the green and NIR regions presented striking increases rather than decreases within the mild DS ranges from 0.0 to 0.2 for anthesis, which did not exhibit a unidirectional weakening as that for the filling stage (Fig. 5B, C).

Determination of optimal bands for constructing the RSRI

Overall, the Spearman correlation between the reflectance of individual bands and DS exhibited consistent trends across the three growth stages (Fig. 4). There were positive correlation domains in the blue and red regions and negative correlation domains in the green and NIR regions. In addition, there was an extra negative correlation domain in the blue region for the heading stage. The correlations were the weakest for the heading stage with the limited DS range. The correlation between the DS and reflectance in the blue region was stronger than that in the green region for heading and filing, whereas this contrast performed reversely for the anthesis stage.

The spearman correlation curves revealed that RSRD severity was most quantifiable in the red region. In addition, consistent correlations occurred in the NIR region for all growth stages. Based on these features, two bands were selected from the red and NIR regions as parts of the equation for RSRI construction, respectively. The optimal bands in the red region were 680 nm for heading and 675 nm for anthesis and filling (Fig. 4). The most sensitive bands in the NIR region were 751 nm, 743 nm, and 734 nm. Therefore, the common band 675 nm in the red region and the NIR band with the median wavelength of 740 nm were determined to fill the RSRI equation. The third band for RSRI was selected

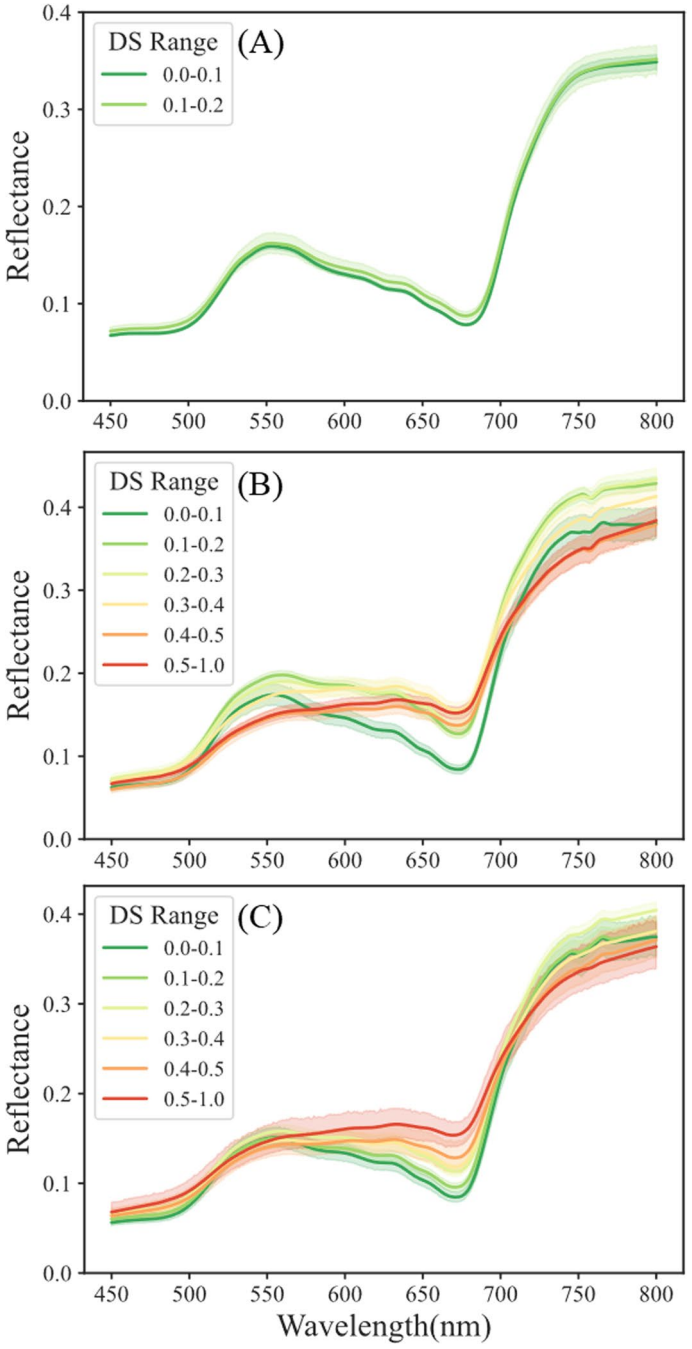

Fig. 5 Reflectance spectra of rice spikelets with various ranges of rice spikelet rot disease (RSRD) severity for a range of growth stages (**A** Heading, **B** Anthesis, **C** Filling). The DS range in (**A**) was narrower due to the low level of inspection allowed at the early infection stage

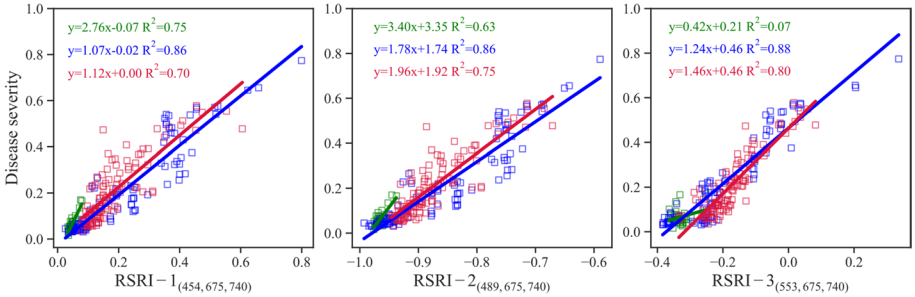

Fig. 6 Relationships between DS and SIs with regression lines and R^2 values. The green, blue, and red squares represent the samples from the heading, anthesis, and filling stages, respectively. All regressions are statistically significant (p value < 0.001) except for the relationship between RSRI-$3_{(553,675,740)}$ and DS for heading (p value = 0.133) (Color figure online)

from the remaining representative bands including 454 nm, 489 nm, and 553 nm for the earliest stage (heading). Three candidate indices with the designations RSRI-1, RSRI-2 and RSRI-3 were built for further comparison.

Obviously, RSRI-1 exhibited a substantially higher correlation with DS than RSRI-2 and RSRI-3 for heading (Fig. 6). For either anthesis or filling, the R^2 values were only slightly different among the three RSRI candidates. Therefore, $RSRI_{454,675,740}$ was determined as the optimal index for the quantification and mapping of DS.

Quantification and mapping of disease severity with RSRI and existing indices

The relationships between DS and SIs varied across stages (Fig. 7). For the heading stage, RSRI yield higher R^2 than other SIs (RSRI: $R^2 = 0.75$; others: $R^2 < 0.66$). For anthesis and filling stages, RSRI exhibited the strongest relationships for both mildly and severely diseased samples. The R^2 for RSRI was close to that for PRI670 and PSRI but higher than that for the remaining SIs. Moreover, the weights of calibrated regression models are different across growth stages for one SI, especially the heading stage. All SIs compared in Fig. 7 exhibited similar phenomenon except for PRI670.

In general, accuracies in DS estimation for each SI varied significantly across the involved growth stages (Figs. 8, 9). The quantification performance was the best for the anthesis stage and the weakest for the heading stage. Besides, RSRI and existing SIs showed contrasting accuracies in DS quantification. For the heading stage, RSRI yielded the best accuracy in DS quantification ($R^2 = 0.65$) (Fig. 8A) and exhibited the most concentrated confidence intervals (CIs) of RMSE and validation R^2 among all five indices (Fig. 9). All existing SIs failed to quantify the DS effectively with significantly wider CIs of the accuracy metrics than RSRI for heading. The results illustrated that the validation R^2 with RSRI for DS quantification were 0.84 and 0.78 (Fig. 8B, C) with compact CIs metrics for anthesis and filling (Fig. 9), respectively. Additionally, underestimation of RSRD severity for the mild range for anthesis occurred to the existing SIs but did not occur to RSRI (Fig. 8). RSRI showed the best performance in DS quantification across growth stages.

Figure 10 displays the spatial variation in DS within spikelets mapped by combining the SI-based linear models and hyperspectral cubes for three representative samples. With the RGB images as references, RSRD infected regions were successfully delineated by the mapping method. However, existing SIs did not generate an authentic mapping of

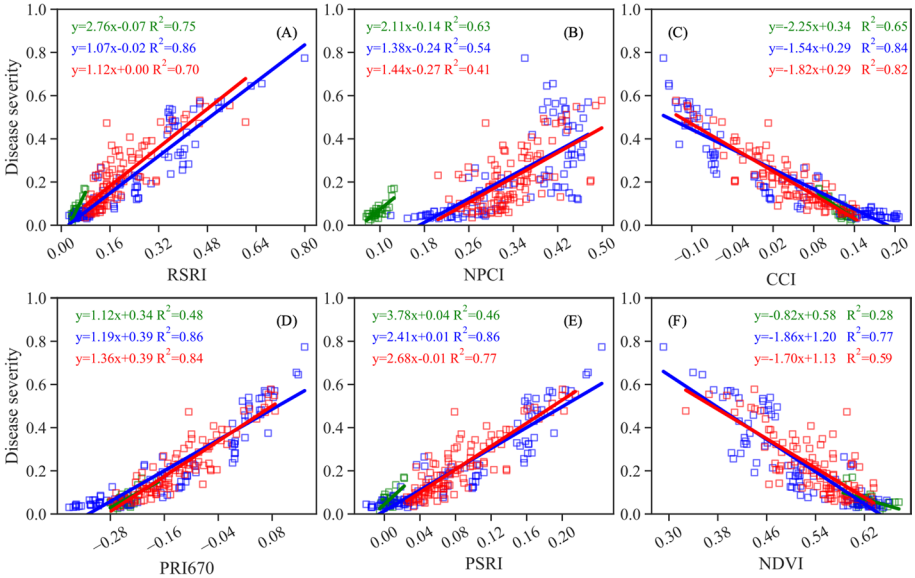

Fig. 7 Relationships between DS and SIs with regression lines and R^2 values. The green, blue, and red squares represent the samples from the heading, anthesis, and filling stages, respectively. All regressions are statistically significant (p value < 0.001) (Color figure online)

DS distribution as the proposed SI did. In contrast, the RSRI-based maps exhibited fewer yellow regions overestimated from the healthy pixels than the selected SIs, whereas these areas were wrongly tagged with mild disease severity (Fig. 10A, B). RSRI-based maps also unveiled the severely diseased areas properly, unlike the weak display of the counterpart lesions based on selected SIs (Fig. 10C). The lesion distribution with RSRI showed the strongest similarity with the reference images, especially for the slightly and severely infected areas.

Discussion

Impact of spikelet ripening on the spectral responses to RSRD infection

The spectral differences across growth stages indicate that the spectral responses of RSRD infected spikes were co-influenced by pathogen–host interactions and spikelet ripening. From a pathology perspective, spectral responses were mainly affected by impairments in biochemical compositions and tissue structures. The reflectance in the visible and NIR regions was linked to the pigment concentration and the leaf internal structure, respectively (Feret et al., 2008). Therefore, the degradation of chlorophyll and carotenoid caused by chlorotic damages from RSRD was responsible for the reflectance increase in the blue and red regions. The reflectance decrease in the green peak (Fig. 11A) could be attributed to the increase in the content of anthocyanin, a defensive pigment sensitive to stresses (Xia et al., 2021). Furthermore, necrotic damages in the form of RSRD penetration into glume tissues (Lei et al., 2019) would be the main reason for the reflectance collapse in the NIR

Fig. 8 Scatter plots of measured and estimated disease severity (DS) with SI-based models for the heading (left column), anthesis (middle column), and filling (right column) stages. The top through the bottom rows represent RSRI (**A–C**), NPCI (**D–F**), CCI (**G–I**), PRI670 (**J–L**), PSRI (**M–O**) and NDVI (**P–R**), respectively

plateau. These findings were consistent with those in relevant studies (Mahlein, 2016; Ren et al., 2021; Tian et al., 2021). From a ripening perspective, the spectral change trends were influenced by biochemical variations with the spikelet development. The chlorophyll content and the carotenoid-to-chlorophyll ratio decrease with growth stages in spikelets (Chen et al., 2006), which should be the physiological basis of the reflectance increase in the red region with the spikelet ripening (Fig. 11B). Although the magnitude of NIR plateau responded significantly to nitrogen content in spikelets (Cheng et al., 2018), the spectral shape remained unchanged (Fig. 11).

Similarities of spectral variation between the disease development and spikelet ripening could weaken the universality in feature construction and DS estimation for multiple growth stages. This influence was proved by the differences in the spectral responses to RSRD and the unbalanced DS quantification accuracy across growth stages. In this regard, earlier research also found different optimal features for multi-growth-stage disease monitoring (Zhang et al., 2020b; Zheng et al., 2018). Moreover, the subtle spectral responses might not outweigh the variation from ripening, which could cause significant estimation errors for samples from the slightly to mildly infection stages as existing SIs did in model validations (Fig. 8). The coexistent influence of stresses and phenological changes is more common for disease detection at the canopy scale (Lassalle, 2021). Hence, it is crucial to ensure the derived spectral features for spikelet disease monitoring were effective across growth stages.

Previous research mitigated the phenological influence in the form of senescence in pathogen examination by extracting features from full-band spectral information with principal component analysis or simple volume maximization (Kuska et al., 2015; Lucas et al., 2021). However, spectral features from transformations might not be suitable for mild infection, since the spectral responses in the red region to RSRD could be similar to that to spikelet ripening for both magnitude and shape. The wavelength regions insensitive to the spikelet growth could be considered to suppress the ripening effect over the full-band transformation. Given the stability of anthocyanin content and the internal structure in healthy spikelets across growth stages for common rice cultivars (Mackon et al., 2021), the spectral variation from ripening could be excluded in the decrease of green reflectance and the unique slope of the NIR region. These disease-specific bands could be used to avoid the influence of spikelet ripening on the performance of disease detection by SIs. Moreover, this issue may be further resolved by using more bands beyond the VNIR region, such as the water content and dry matter sensitive bands in the shortwave infrared region (Tian et al., 2021; Yan et al., 2021). However, such ripening-insensitive bands are not qualified in DS estimation for the early infection stage according to the SI comparison. The bands sensitive to early infection should also be determined to increase the accuracy consistency in DS estimation for both the early stage of infection and multiple growth stages.

Contribution of blue bands to disease monitoring

The importance of blue bands could be supported by the fact that only RSRI and NPCI achieved acceptable accuracy in DS quantification for the heading stage (the early

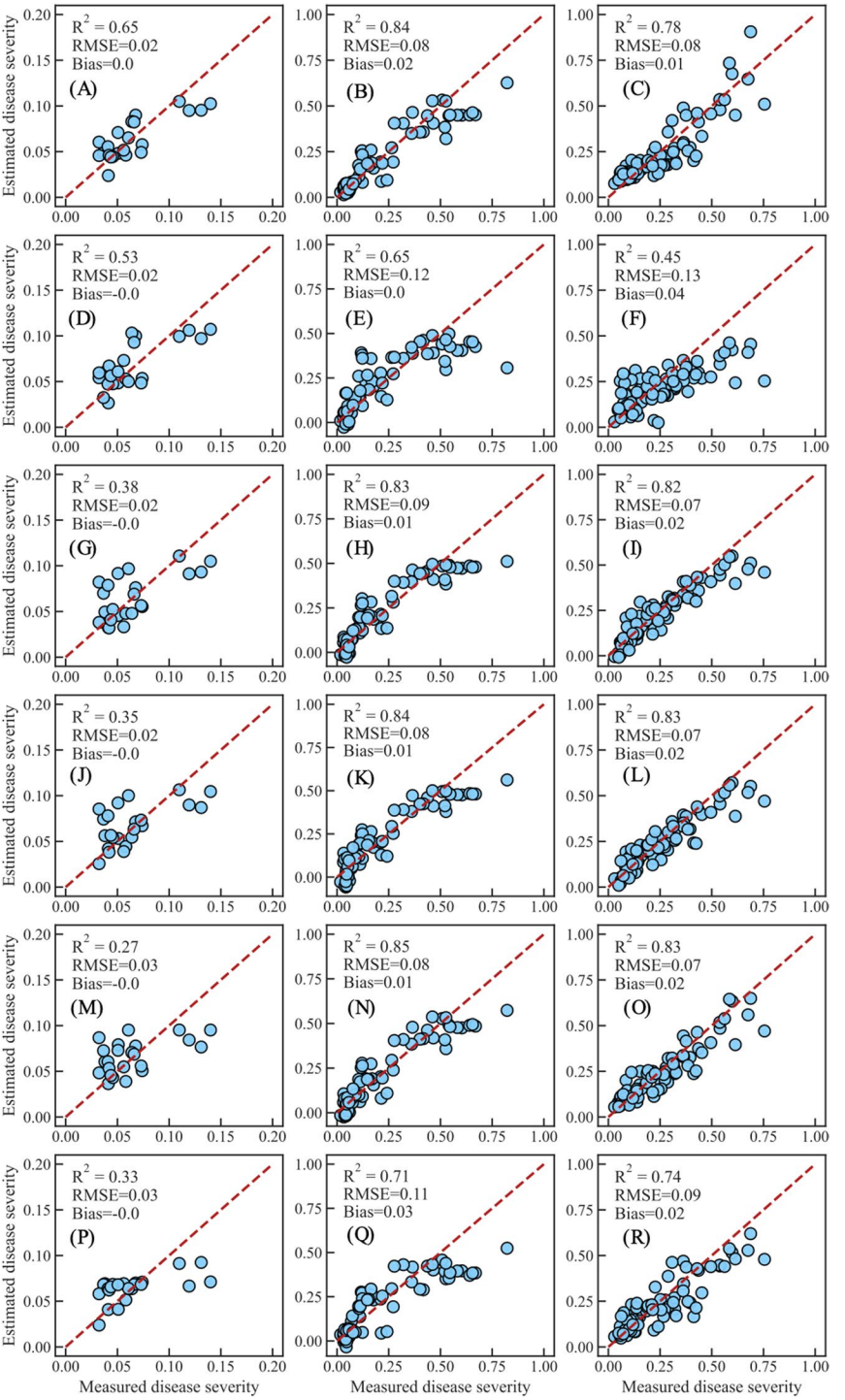
(A) R² = 0.65 RMSE=0.02 Bias=0.0
(B) R² = 0.84 RMSE=0.08 Bias=0.02
(C) R² = 0.78 RMSE=0.08 Bias=0.01
(D) R² = 0.53 RMSE=0.02 Bias=-0.0
(E) R² = 0.65 RMSE=0.12 Bias=0.0
(F) R² = 0.45 RMSE=0.13 Bias=0.04
(G) R² = 0.38 RMSE=0.02 Bias=-0.0
(H) R² = 0.83 RMSE=0.09 Bias=0.01
(I) R² = 0.82 RMSE=0.07 Bias=0.02
(J) R² = 0.35 RMSE=0.02 Bias=-0.0
(K) R² = 0.84 RMSE=0.08 Bias=0.01
(L) R² = 0.83 RMSE=0.07 Bias=0.02
(M) R² = 0.27 RMSE=0.03 Bias=-0.0
(N) R² = 0.85 RMSE=0.08 Bias=0.01
(O) R² = 0.83 RMSE=0.07 Bias=0.02
(P) R² = 0.33 RMSE=0.03 Bias=-0.0
(Q) R² = 0.71 RMSE=0.11 Bias=0.03
(R) R² = 0.74 RMSE=0.09 Bias=0.02
Estimated disease severity
Measured disease severity

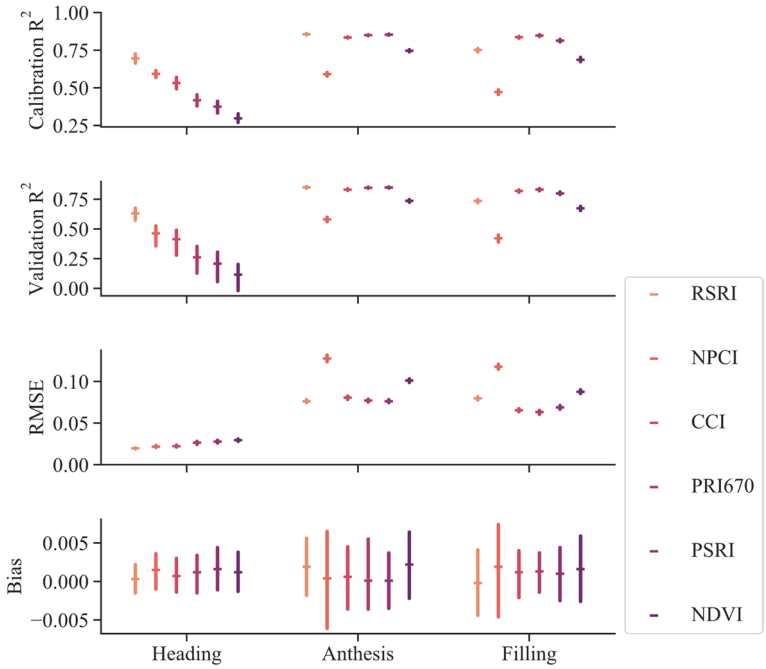

Fig. 9 Comparison of calibration accuracies (R^2), validation accuracies (R^2), RMSE, and bias for RSRI and existing SIs in DS (disease severity) quantification over various stages (left column: heading, middle column: anthesis, right column: filling). The average value (horizontal bars) of one hundred rounds of evaluations is accompanied by confidence intervals (vertical bars)

stage of infection) among involved SIs. The reflectance in the blue region is characterized by the overlapping absorption of major pigments (Feret et al., 2008). Therefore, the blue reflectance should be sensitive to subtle biochemical changes caused by pathogen infections. For instance, the blue spectral features could record the decreases in chlorophyll content that are often observed in the senescent and unhealthy plants at the early stressed stage (Peñuelas et al., 1995). The merits of blue bands in disease monitoring at the early infection were also highlighted in previous studies (Brugger et al., 2019; Poblete et al., 2020; Zarco-Tejada et al., 2018). Moreover, the insensitivity of blue bands to the spikelet ripening could partially explain the consistent sensitivity of RSRI to DS across growth stages (Figs. 7, 8).

To understand the effect of bandwidth in disease monitoring, new RSRIs were derived from the broad spectral bands simulated according to the Airphen (Hi-phen, France) and RedEdge-MX multispectral cameras (Micasense, USA), which are commonly mounted on unmanned aerial vehicles in vegetation remote sensing. Following Soudani et al., (2006), the broad-band reflectance was calculated based on the integration of the spectral response functions of the sensors and the hyperspectral reflectance. Compared to the narrow-band RSRI, the broad-band ones displayed similar relationships between DS and SI, and performance in RSRD severity quantification for multiple growth stages (Figs. 12, 13). Such performance suggests broad blue bands are also efficient in DS estimation and they are promising in disease monitoring with cameras mounted on UAVs. Yet blue features might

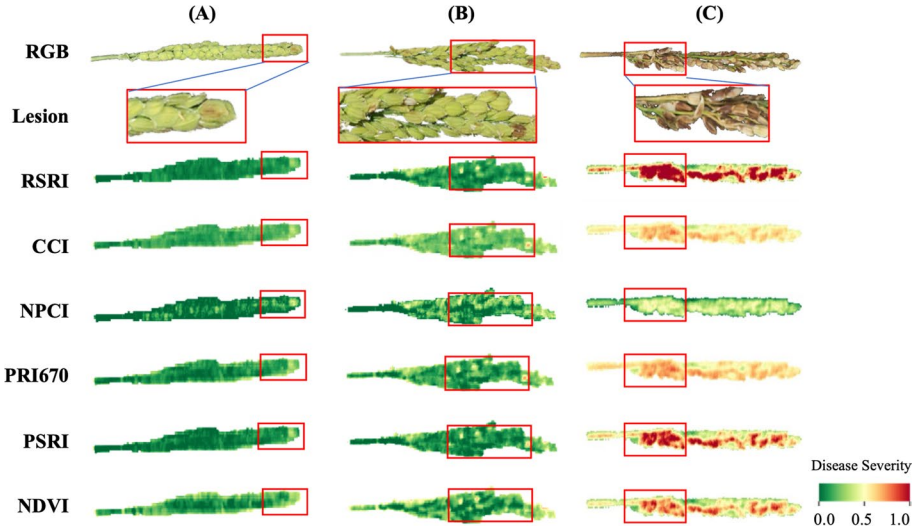

Fig. 10 RGB images, lesion distribution reference, and DS maps derived from RSRI and existing SIs for three independent spikelet samples (**A** a slightly infected spikelet, **B** a mildly infected spikelet, and **C** a severely infected spikelet). Note that the small gaps between grains can be identified on the RGB images but cannot be separated on the hyperspectral images due to their low spatial resolution

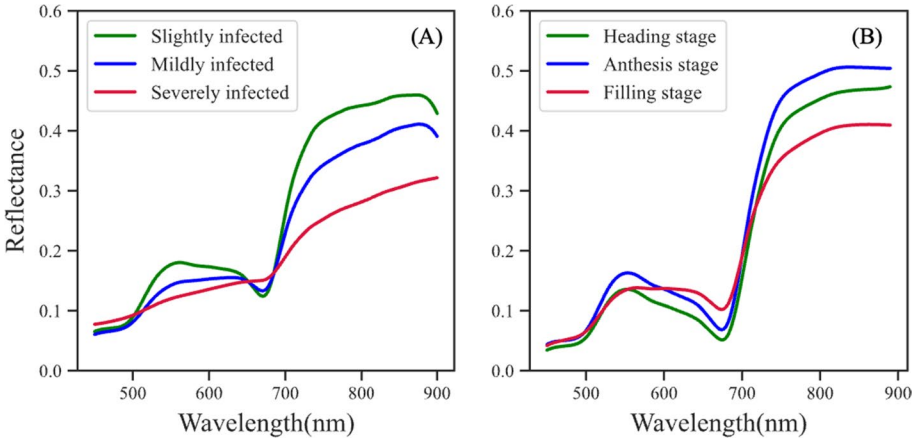

Fig. 11 **A** Reflectance spectra of three spikelets with various RSRD severities for the anthesis stage. **B** represents the reflectance spectra of three healthy rice spikelets independent of this study for the heading, anthesis, and filling stages, respectively

not be suitable for aerial or spaceborne platforms due to the atmospheric effect (Li et al., 2020).

However, the blue reflectance variation is hard to understand by linking the biochemical variation since it is affected by the complex degradation of pigments (Feret et al., 2008). Although blue bands might not be competent for disease monitoring individually because of the weak sensitivity to DS in contrast with red bands (Fig. 4), feature engineering

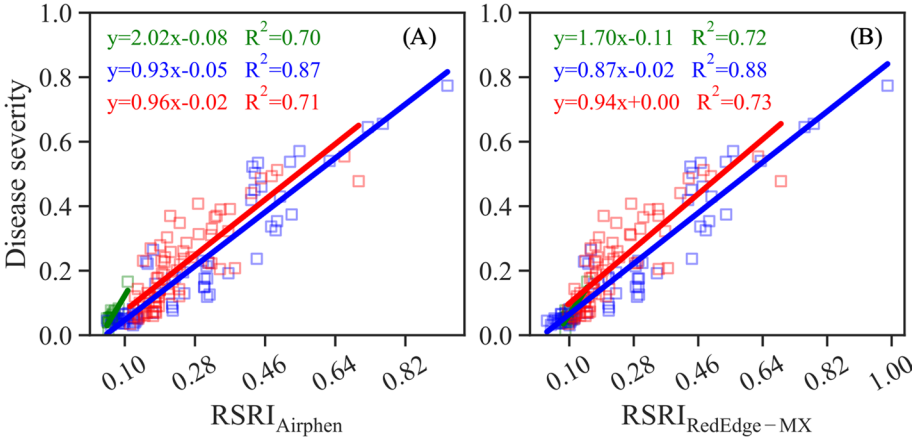

Fig. 12 The DS–RSRI relationships for three growth stages with the simulated **A** Airphen and **B** RedEdge-MX data. Green, blue, and the red squares represent the samples from heading, anthesis, and filling stages, respectively. RSRI was calculated from multispectral reflectance simulated with hyperspectral cubes by referring to the bandwidth and center wavelength of Airphen or RedEdge-MX. The bands 454 nm, 675 nm, and 740 nm were replaced by the blue, red, and near-infrared bands for each sensor. All regressions are statistically significant (p value < 0.001) (Color figure online)

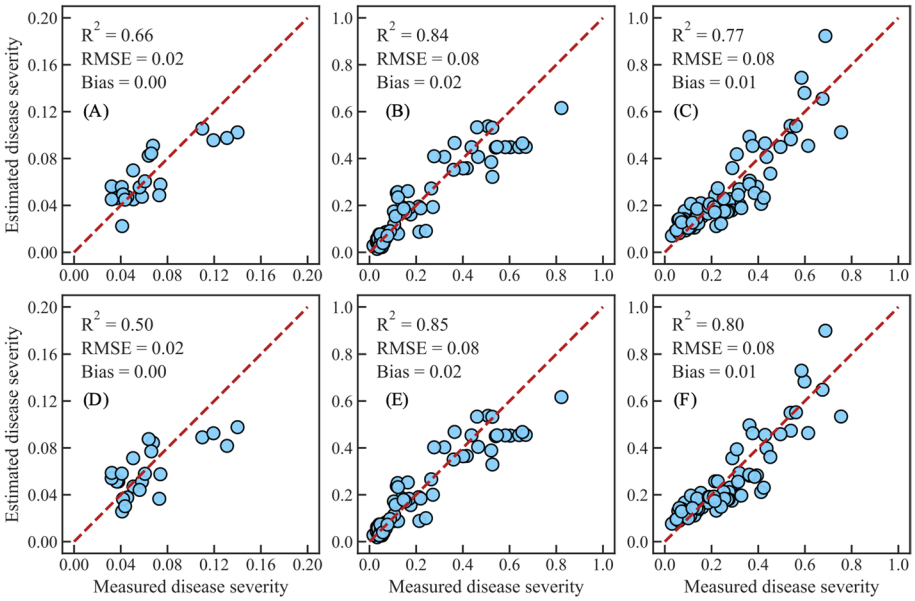

Fig. 13 Scatter plots of measured and estimated quantified DS (disease severity) with RSRI-based models derived from multispectral data (**A**–**C** Airphen camera, **D**–**F** RedEdge-MX camera) for the heading (**A**, **D**), anthesis (**B**, **E**), and filling (**C**, **F**) stages

approaches could be used to magnify the sensitivity of blue bands such as SIs, feature combinations, and spectral transformations applied in previous studies (Tian et al., 2021; Zarco-Tejada et al., 2018). Moreover, the subtle biochemical changes hidden behind the

blue band response could be different according to the pathogen categories (Poblete et al., 2020). Determination of specific band regions sensitive to a certain stress is crucial for the feature construction in DS estimation and disease identification.

Implications and prospects

A few studies have constructed SIs or feature sets for spikelet disease monitoring with remote sensing (Huang et al., 2015; Mahlein et al., 2019a; Zhang et al., 2020b). However, these studies may have neglected the consistence in sensitivity over multiple growth stages or a wide range of disease severities due to the limited measurements within a short period of growth. For example, significant underestimation for mildly diseased samples was observed in the detection of wheat Fusarium Head Blight by Zhang et al. (2020b). Results in this study indicated that the SIs insensitive to the slight-to-mild DS for anthesis were poorly related to DS for heading (Figs. 7, 8). In contrast, RSRI-based models showed the most stable performance for all involved growth stages in DS estimation, as well as the models with broadband-based RSRIs. Therefore, it is encouraging to monitor the DS from RSRI with affordable sensors.

Moreover, the mapping results demonstrated that pathogen colonies could be revealed properly in the RSRI-based severity maps, which were more distinct than the RGB reference. These non-invasive observations could facilitate the investigation of the spatial and temporal patterns of pathogen–host interactions. Such ability of HSI has been proven superior to various validation approaches including genetic tests, microscope tests, and temporal comparisons for living hosts (Brugger et al., 2021; Tian et al., 2021; Zarco-Tejada et al., 2018). Further work would include time-series validation to solidify the mechanistic understanding of pathology and spectroscopy.

As for spikelet disease monitoring, more challenges need to be faced due to the complexity of the reproductive organs in morphology and geometry except for the ripening influence. Although a study found no significant difference between the front and rear sides of spikelets in DS estimation (Zhang et al., 2020a, 2020b), infected crop spikelets are three-dimensional organs with different lesion distributions on the sides, which requires full observations to evaluate the disease condition. Secondly, it is hard to obtain a clear view of reproductive organs during the spectral imaging phase at the canopy scale due to the variable poses and severe overlaps of spikelets. Previous studies found larger viewing angles resulted in higher accuracies in DS estimation with more target information (Gu et al., 2021; He et al., 2021; Oberti et al., 2014) In phenotyping and breeding activities, however, one-side or single-angle imaging with partial optical information may be inadequate to make reliable decisions. Multi-angular measurements could enhance the signal for disease monitoring at the canopy scale, although, the pre-processing procedures including multi-angular image matching may still be at a high cost.

Conclusion

This study determined the differences in spectral responses to RSRD among multiple growth stages and constructed a new index, RSRI, sensitive to RSRD across multiple phenological stages. The results indicated that the sensitivities of reflectance in the green and near-infrared regions to DS for filling were significantly lower than those for

anthesis. RSRI optimization showed that the addition of blue bands increased the SI sensitivity to DS for heading, enhancing the early disease detection. Compared with NPCI, CCI, PRI670, PSRI, and NDVI, RSRI exhibited the highest sensitivity to DS at the early infection stage and the most stable performance from heading to grain filling in DS estimation (Heading: $R^2 = 0.65$, RMSE = 0.02; anthesis: $R^2 = 0.84$, RMSE = 0.08 for; filling: $R^2 = 0.78$, RMSE = 0.08). Moreover, the RSRI-based model mapped the lesion distribution more properly than the previous studied SIs for slightly, mildly, and severely diseased samples. The DS estimation and the lesion mapping of the RSRD at the early infection stage could provide an effective reference in crop protection and pathology research.

Acknowledgements This work was supported by the National Key R&D Program of China (2021YFE0194800), National Natural Science Foundation of China (41871259) and Collaborative Innovation Center for Modern Crop Production co-sponsored by Ministry and Province. We are especially grateful to Dr. Shiwen Huang for his instruction in visual identification of RSRD. We would like to thank Pengzhi Liu, Zhonghua Li, and Wenhui Wang for their assistance in the field experiments and data acquisition. We would also like to thank the anonymous reviewers who provide helpful comments to improve the manuscript.

Declarations

Conflict of interest The authors declare that they have no conflict of interest.

References

Brugger, A., Behmann, J., Paulus, S., Luigs, H. G., Kuska, M. T., Schramowski, P., et al. (2019). Extending hyperspectral imaging for plant phenotyping to the UV-range. *Remote Sensing*, *11*(12), 1401. https://doi.org/10.3390/rs11121401.

Brugger, A., Schramowski, P., Paulus, S., Steiner, U., Kersting, K., & Mahlein, A. (2021). Spectral signatures in the UV range can be combined with secondary plant metabolites by deep learning to characterize barley–powdery mildew interaction. *Plant Pathology*, *70*(7), 1572–1582. https://doi.org/10.1111/ppa.13411.

Chen, W., Zhou, Q., & Huang, J. F. (2006). Estimating pigment contents in leaves and panicles of rice after milky ripening by hyperspectral vegetation indices. *Chineses Journal of Rice Science, 20*(4), 434. https://doi.org/10.16819/j.1001-7216.2006.04.017

Cheng, T., Zhu, Y., Li, D., Yao, X., & Zhou, K. (2018). Hyperspectral remote sensing of leaf nitrogen concentration in cereal crops. In P. S. Thenkabail, J. G. Lyon, & A. Huete (Eds.), *Hyperspectral indices and image classifications for agriculture and vegetation* (2nd ed., pp. 163–182). CRC Press. https://doi.org/10.1201/9781315159331-6

Feng, Z. H., Wang, L. Y., Yang, Z. Q., Zhang, Y. Y., Li, X., Song, L., et al. (2022). Hyperspectral monitoring of Powdery Mildew Disease Severity in Wheat based on machine learning. *Frontiers in Plant Science*, *13*, 828454. https://doi.org/10.3389/fpls.2022.828454.

Feret, J. B., François, C., Asner, G. P., Gitelson, A. A., Martin, R. E., Bidel, L. P. R., et al. (2008). PROSPECT-4 and 5: Advances in the leaf optical properties model separating photosynthetic pigments. *Remote Sensing of Environment, 112*(6), 3030–3043. https://doi.org/10.1016/j.rse.2008.02.012

Gamon, J. A., Huemmrich, K. F., Wong, C. Y. S., Ensminger, I., Garrity, S., Hollinger, D. Y., et al. (2016). A remotely sensed pigment index reveals photosynthetic phenology in evergreen conifers. *Proceedings of the National Academy of Sciences*, *113*(46), 13087–13092. https://doi.org/10.1073/pnas.1606162113

Gamon, J. A., Peñuelas, J., & Field, C. B. (1992). A narrow-waveband spectral index that tracks diurnal changes in photosynthetic efficiency. *Remote Sensing of Environment*, *41*(1), 35–44. https://doi.org/10.1016/0034-4257(92)90059-S.

Gao, Z., Zhao, Y., Khot, L. R., Hoheisel, G. A., & Zhang, Q. (2019). Optical sensing for early spring freeze related blueberry bud damage detection: Hyperspectral imaging for salient spectral wavelengths identification. *Computers and Electronics in Agriculture, 167*, 105025. https://doi.org/10.1016/j.compag.2019.105025

Gold, K. M., Townsend, P. A., Chlus, A., Herrmann, I., Couture, J. J., Larson, E. R., & Gevens, A. J. (2020). Hyperspectral measurements enable pre-symptomatic detection and differentiation of contrasting physiological effects of late blight and early blight in Potato. *Remote Sensing, 12*(2), 286. https://doi.org/10.3390/rs12020286

Gonzalez, R. C., & Woods, R. E. (2002). *Digital image processing* (2nd ed.). Prentice Hall. Retrieved 20 June, 2021, from https://book.douban.com/subject/1868037/.

Gu, C., Wang, D., Zhang, H., Zhang, J., Zhang, D., & Liang, D. (2021). Fusion of Deep Convolution and shallow features to recognize the severity of wheat Fusarium Head Blight. *Frontiers in Plant Science*, *11*, 599886. https://doi.org/10.3389/fpls.2020.599886.

He, L., Qi, S. L., Duan, J. Z., Guo, T. C., Feng, W., & He, D. X. (2021). Monitoring of wheat powdery mildew disease severity using multiangle hyperspectral remote sensing. *IEEE Transactions on Geoscience and Remote Sensing*, *59*(2), 979–990. https://doi.org/10.1109/TGRS.2020.3000992.

Hornero, A., Hernández-Clemente, R., North, P. R. J., Beck, P. S. A., Boscia, D., Navas-Cortes, J. A., & Zarco-Tejada, P. J. (2020). Monitoring the incidence of Xylella fastidiosa infection in olive orchards using ground-based evaluations, airborne imaging spectroscopy and Sentinel-2 time series through 3-D radiative transfer modelling. *Remote Sensing of Environment*, *236*, 111480. https://doi.org/10.1016/j.rse.2019.111480.

Huang, S., Qi, L., Ma, X., Xue, K., Wang, W., & Zhu, X. (2015). Hyperspectral image analysis based on BoSW model for rice panicle blast grading. *Computers and Electronics in Agriculture*, *118*, 167–178. https://doi.org/10.1016/j.compag.2015.08.031.

Huang, S. W., Wang, L., Liu, L. M., Tang, S. Q., Zhu, D. F., & Savary, S. (2011a). Rice spikelet rot disease in China—1. Characterization of fungi associated with the disease. *Crop Protection*, *30*(1), 1–9. https://doi.org/10.1016/j.cropro.2010.07.010.

Huang, S. W., Wang, L., Liu, L. M., Tang, S. Q., Zhu, D. F., & Savary, S. (2011b). Rice spikelet rot disease in China—2. Pathogenicity tests, assessment of the importance of the disease, and preliminary evaluation of control options. *Crop Protection*, *30*(1), 10–17. https://doi.org/10.1016/j.cropro.2010.06.008.

Huo, L., Persson, H. J., & Lindberg, E. (2021). Early detection of forest stress from European spruce bark beetle attack, and a new vegetation index: Normalized distance red & SWIR (NDRS). *Remote Sensing of Environment*, *255*, 112240. https://doi.org/10.1016/j.rse.2020.112240.

Jagadish, S. V. K., Murty, M. V. R., & Quick, W. P. (2015). Rice responses to rising temperatures—challenges, perspectives and future directions. *Plant Cell & Environment*, *38*(9), 1686–1698. https://doi.org/10.1111/pce.12430.

Kobayashi, T., Sasahara, M., Kanda, E., Ishiguro, K., Hase, S., & Torigoe, Y. (2016). Assessment of rice panicle blast disease using airborne hyperspectral imagery. *The Open Agriculture Journal*, *10*(1), 28–34. https://doi.org/10.2174/1874331501610010028.

Kochubey, S. M., & Kazantsev, T. A. (2012). Derivative vegetation indices as a new approach in remote sensing of vegetation. *Frontiers of Earth Science*, *6*(2), 188–195. https://doi.org/10.1007/s11707-012-0325-z.

Kuska, M., Wahabzada, M., Leucker, M., Dehne, H. W., Kersting, K., Oerke, E. C., et al. (2015). Hyperspectral phenotyping on the microscopic scale: Towards automated characterization of plant-pathogen interactions. *Plant Methods*, *11*(1), 28. https://doi.org/10.1186/s13007-015-0073-7.

Lassalle, G. (2021). Monitoring natural and anthropogenic plant stressors by hyperspectral remote sensing: Recommendations and guidelines based on a meta-review. *Science of the Total Environment*, *788*, 147758. https://doi.org/10.1016/j.scitotenv.2021.147758.

Lei, S., Wang, L., Liu, L., Hou, Y., Xu, Y., Liang, M., et al. (2019). Infection and colonization of pathogenic Fungus Fusarium proliferatum in rice spikelet rot disease. *Rice Science*, *26*(1), 60–68. https://doi.org/10.1016/j.rsci.2018.08.005.

Li, D., Chen, J. M., Zhang, X., Yan, Y., Zhu, J., Zheng, H., et al. (2020). Improved estimation of leaf chlorophyll content of row crops from canopy reflectance spectra through minimizing canopy structural effects and optimizing off-noon observation time. *Remote Sensing of Environment*, *248*, 111985. https://doi.org/10.1016/j.rse.2020.111985.

Li, D., Tian, L., Wan, Z., Jia, M., Yao, X., Tian, Y., et al. (2019). Assessment of unified models for estimating leaf chlorophyll content across directional-hemispherical reflectance and bidirectional reflectance spectra. *Remote Sensing of Environment*, *231*, 111240. https://doi.org/10.1016/j.rse.2019.111240.

Liu, W., Liu, J., Triplett, L., Leach, J. E., & Wang, G. L. (2014). Novel insights into rice innate immunity against bacterial and fungal pathogens. In N. K. VanAlfen (Ed.), *Annual review of phytopathology,* (Vol. 52, pp. 213–241). Annual Reviews. https://doi.org/10.1146/annurev-phyto-102313-045926

Lucas, D., da Silva, A., Alves Filho, E. G., Silva, L. M. A., Huertas Tavares, C., Gervasio Pereira, O., de Campos, M., T., & da Silva, M., L (2021). Near infrared spectroscopy to rapid assess the rubber tree

clone and the influence of maturation and disease at the leaves. *Microchemical Journal*, *168*, 106478. https://doi.org/10.1016/j.microc.2021.106478.

Mackon, E., Mackon, J. D. E., Ma, G. C., Haneef Kashif, Y., Ali, M., Usman, N., B., & Liu, P. (2021). Recent insights into anthocyanin pigmentation, synthesis, trafficking, and regulatory mechanisms in rice (*Oryza sativa* L.) Caryopsis. *Biomolecules*, *11*(3), 394. https://doi.org/10.3390/biom11030394.

Mahlein, A. K. (2016). Plant disease detection by imaging sensors—parallels and specific demands for precision agriculture and plant phenotyping. *Plant Disease*, *100*(2), 241–251. https://doi.org/10.1094/PDIS-03-15-0340-FE.

Mahlein, A. K., Alisaac, E., Al Masri, A., Behmann, J., Dehne, H. W., & Oerke, E. C. (2019a). Comparison and combination of thermal, fluorescence, and hyperspectral imaging for monitoring fusarium head blight of wheat on spikelet scale. *Sensors, 19*(10), 2281. https://doi.org/10.3390/s19102281.

Mahlein, A. K., Kuska, M. T., Thomas, S., Wahabzada, M., Behmann, J., Rascher, U., & Kersting, K. (2019b). Quantitative and qualitative phenotyping of disease resistance of crops by hyperspectral sensors: Seamless interlocking of phytopathology, sensors, and machine learning is needed!. *Current Opinion in Plant Biology, 50*, 156–162. https://doi.org/10.1016/j.pbi.2019b.06.007.

Mahlein, A.-K., Rumpf, T., Welke, P., Dehne, H.-W., Plümer, L., Steiner, U., & Oerke, E.-C. (2013). Development of spectral indices for detecting and identifying plant diseases. *Remote Sensing of Environment, 128*, 21–30. https://doi.org/10.1016/j.rse.2012.09.019

Meng, R., Gao, R., Zhao, F., Huang, C., Sun, R., Lv, Z., & Huang, Z. (2022). Landsat-based monitoring of southern pine beetle infestation severity and severity change in a temperate mixed forest. *Remote Sensing of Environment*, *269*, 112847. https://doi.org/10.1016/j.rse.2021.112847.

Merzlyak, M. N., Gitelson, A. A., Chivkunova, O. B., & Rakitin, V. Y. (1999). Non-destructive optical detection of pigment changes during leaf senescence and fruit ripening. *Physiologia Plantarum*, *106*(1), 135–141. https://doi.org/10.1034/j.1399-3054.1999.106119.x.

Morel, J., Jay, S., Féret, J. B., Bakache, A., Bendoula, R., Carreel, F., & Gorretta, N. (2018). Exploring the potential of PROCOSINE and close-range hyperspectral imaging to study the effects of fungal diseases on leaf physiology. *Scientific Reports*, *8*(1), 15933. https://doi.org/10.1038/s41598-018-34429-0.

Oberti, R., Marchi, M., Tirelli, P., Calcante, A., Iriti, M., & Borghese, A. N. (2014). Automatic detection of powdery mildew on grapevine leaves by image analysis: Optimal view-angle range to increase the sensitivity. *Computers and Electronics in Agriculture*, *104*, 1–8. https://doi.org/10.1016/j.compag.2014.03.001.

Oerke, E. C. (2020). Remote sensing of diseases. *Annual Review of Phytopathology*, *58*(1), 225–252. https://doi.org/10.1146/annurev-phyto-010820-012832.

Peñuelas, J., Filella, I., Lloret, P., Mun¯Oz, F., & Vilajeliu, M. (1995). Reflectance assessment of mite effects on apple trees. *International Journal of Remote Sensing*, *16*(14), 2727–2733. https://doi.org/10.1080/01431169508954588.

Peñuelas, J., Gamon, J. A., Griffin, K. L., & Field, C. B. (1993). Assessing community type, plant biomass, pigment composition, and photosynthetic efficiency of aquatic vegetation from spectral reflectance. *Remote Sensing of Environment*, *46*(2), 110–118. https://doi.org/10.1016/0034-4257(93)90088-F.

Poblete, T., Camino, C., Beck, P. S. A., Hornero, A., Kattenborn, T., Saponari, M., et al. (2020). Detection of Xylella fastidiosa infection symptoms with airborne multispectral and thermal imagery: Assessing bandset reduction performance from hyperspectral analysis. *ISPRS Journal of Photogrammetry and Remote Sensing*, *162*, 27–40. https://doi.org/10.1016/j.isprsjprs.2020.02.010.

Ren, Y., Huang, W., Ye, H., Zhou, X., Ma, H., Dong, Y., et al. (2021). Quantitative identification of yellow rust in winter wheat with a new spectral index: Development and validation using simulated and experimental data. *International Journal of Applied Earth Observation and Geoinformation*, *102*, 102384. https://doi.org/10.1016/j.jag.2021.102384.

Rouse, J. W., Haas, R. H., Deering, D. W., Schell, J. A., Harlan, J. C., Haas, R. H., et al. (1974). Monitoring the vernal advancement and retrogradation (Green Wave Effect) of natural vegetation. Retrieved June 3, 2022, from https://ntrs.nasa.gov/citations/19750020419.

Ruan, C., Dong, Y., Huang, W., Huang, L., Ye, H., Ma, H., et al. (2021). Prediction of wheat stripe rust occurrence with Time Series Sentinel-2 images. *Agriculture*, *11*(11), 1079. https://doi.org/10.3390/agriculture11111079.

Singh, A., Jones, S., Ganapathysubramanian, B., Sarkar, S., Mueller, D., Sandhu, K., & Nagasubramanian, K. (2021). Challenges and opportunities in machine-augmented plant stress phenotyping. *Trends in Plant Science*, *26*(1), 53–69. https://doi.org/10.1016/j.tplants.2020.07.010.

Soudani, K., François, C., le Maire, G., Le Dantec, V., & Dufrêne, E. (2006). Comparative analysis of IKONOS, SPOT, and ETM + data for leaf area index estimation in temperate coniferous and

deciduous forest stands. *Remote Sensing of Environment*, *102*(1), 161–175. https://doi.org/10.1016/j.rse.2006.02.004.

Tian, L., Xue, B., Wang, Z., Li, D., Yao, X., Cao, Q., et al. (2021). Spectroscopic detection of rice leaf blast infection from asymptomatic to mild stages with integrated machine learning and feature selection. *Remote Sensing of Environment*, *257*, 112350. https://doi.org/10.1016/j.rse.2021.112350.

Xia, D., Zhou, H., Wang, Y., Li, P., Fu, P., Wu, B., & He, Y. (2021). How rice organs are colored: The genetic basis of anthocyanin biosynthesis in rice. *Crop Journal*, *9*(3), 598–608. https://doi.org/10.1016/j.cj.2021.03.013.

Yan, Y., Zhang, X., Li, D., Zheng, H., Yao, X., Zhu, Y., et al. (2021). Laboratory shortwave infrared reflectance spectroscopy for estimating grain protein content in rice and wheat. *International Journal of Remote Sensing*, *42*(12), 4467–4492. https://doi.org/10.1080/01431161.2021.1895450.

Zarco-Tejada, P. J., Camino, C., Beck, P. S. A., Calderon, R., Hornero, A., Hernández-Clemente, R., et al. (2018). Previsual symptoms of Xylella fastidiosa infection revealed in spectral plant-trait alterations. *Nature Plants*, *4*(7), 432–439. https://doi.org/10.1038/s41477-018-0189-7.

Zarco-Tejada, P. J., Poblete, T., Camino, C., Gonzalez-Dugo, V., Calderon, R., Hornero, A., et al. (2021). Divergent abiotic spectral pathways unravel pathogen stress signals across species. *Nature Communications*, *12*(1), 6088. https://doi.org/10.1038/s41467-021-26335-3.

Zhang, D., Chen, G., Yin, X., Hu, R. J., Gu, C. Y., Pan, Z. G., et al. (2020a). Integrating spectral and image data to detect Fusarium head blight of wheat. *Computers and Electronics in Agriculture, 175*, 105588. https://doi.org/10.1016/j.compag.2020c.105588.

Zhang, D., Wang, Q., Lin, F., Yin, X., Gu, C., & Qiao, H. (2020b). Development and evaluation of a new spectral disease index to detect wheat fusarium head blight using hyperspectral imaging. *Sensors*, *20*(8), 2260. https://doi.org/10.3390/s20082260.

Zhang, J., Huang, Y., Pu, R., Gonzalez-Moreno, P., Yuan, L., Wu, K., & Huang, W. (2019). Monitoring plant diseases and pests through remote sensing technology: A review. *Computers and Electronics in Agriculture*, *165*, 104943. https://doi.org/10.1016/j.compag.2019.104943.

Zheng, Q., Huang, W., Cui, X., Dong, Y., Shi, Y., Ma, H., & Liu, L. (2018). Identification of wheat yellow rust using Optimal Three-Band Spectral Indices in different growth stages. *Sensors*, *19*(1), 35. https://doi.org/10.3390/s19010035.

Zheng, Q., Ye, H., Huang, W., Dong, Y., Jiang, H., Wang, C., et al. (2021). Integrating spectral information and meteorological data to monitor wheat yellow rust at a regional scale: a case study. *Remote Sensing*, *13*(2), 278. https://doi.org/10.3390/rs13020278.

Zhou, K., Cheng, T., Zhu, Y., Cao, W., Ustin, S. L., Zheng, H., et al. (2018). Assessing the impact of spatial resolution on the estimation of leaf nitrogen concentration over the full season of paddy rice using near-surface imaging spectroscopy data. *Frontiers in Plant Science*, *9*, 964. https://doi.org/10.3389/fpls.2018.00964.

Zhou, X., Zheng, H. B., Xu, X. Q., He, J. Y., Ge, X. K., Yao, X., et al. (2017). Predicting grain yield in rice using multi-temporal vegetation indices from UAV-based multispectral and digital imagery. *ISPRS Journal of Photogrammetry and Remote Sensing*, *130*, 246–255. https://doi.org/10.1016/j.isprsjprs.2017.05.003.